



This is a repository copy of *Turbulent mean flow reconstruction based on sparse multi-sensor data and adjoint-based field inversion*.

White Rose Research Online URL for this paper:
<https://eprints.whiterose.ac.uk/188729/>

Version: Accepted Version

Proceedings Paper:

Bidar, O., He, P., Anderson, S. orcid.org/0000-0002-7452-5681 et al. (1 more author) (2022) Turbulent mean flow reconstruction based on sparse multi-sensor data and adjoint-based field inversion. In: AIAA AVIATION 2022 Forum. AIAA AVIATION 2022 Forum, 27 Jun - 01 Jul 2022, Chicago, IL, USA (and online). AIAA Aviation Forum Proceedings . American Institute of Aeronautics and Astronautics .

<https://doi.org/10.2514/6.2022-3900>

© 2022 by Omid Bidar. Published by the American Institute of Aeronautics and Astronautics, Inc.. This is an author-produced version of a paper subsequently published in AIAA AVIATION 2022 Forum. Uploaded in accordance with the publisher's self-archiving policy.

Reuse

Items deposited in White Rose Research Online are protected by copyright, with all rights reserved unless indicated otherwise. They may be downloaded and/or printed for private study, or other acts as permitted by national copyright laws. The publisher or other rights holders may allow further reproduction and re-use of the full text version. This is indicated by the licence information on the White Rose Research Online record for the item.

Takedown

If you consider content in White Rose Research Online to be in breach of UK law, please notify us by emailing eprints@whiterose.ac.uk including the URL of the record and the reason for the withdrawal request.



eprints@whiterose.ac.uk
<https://eprints.whiterose.ac.uk/>

Turbulent Mean Flow Reconstruction Based on Sparse Multi-sensor Data and Adjoint-based Field Inversion

Omid Bidar^{*1}, Ping He^{†2}, Sean Anderson^{‡1}, and Ning Qin^{§1}

¹*The University of Sheffield, Western Bank, Sheffield, S10 2TN, UK*

²*Iowa State University, Ames, Iowa, 50011, USA*

There is significant interest in using limited, experimentally measurable, data to reconstruct turbulent mean flows. One approach to achieve this is field inversion, which involves introducing a spatially varying field in the transport equation of the turbulence model, and optimising this field such that the error between the data and model predictions is minimised. This highly dimensional inverse problem is solved with gradient-based optimisation, driven by efficient derivative computations of the cost function using the adjoint method. It has been used to achieve promising results using limited observations from one data source, such as lift force, surface friction etc. In practice, experimental data are often disparate in nature: various quantities from different parts of the flow domain, with varying dimensions and quality. In this work, we will investigate the use of field inversion with disparate data based on sensor fusion and the solution of a multi-objective optimisation, for augmenting the Spalart–Allmaras turbulence model. The separated flows over the NASA wall-mounted hump and the periodic hill are used as test cases, with datasets comprising of velocity profiles, surface pressure, and surface friction. Results highlight improved mean flow reconstruction when incorporating multiple quantities.

I. Introduction

Turbulence is a ubiquitous flow phenomenon in aerospace applications, and is generally investigated using experiments and/or computational fluid dynamics (CFD). In both approaches, limitations exist in terms of the level of fidelity and costs. By far the most used models in practical CFD analyses are based on Reynolds-averaged Navier–Stokes (RANS) equations, due to their relative simplicity, low computational cost, and ease of implementation. RANS equations require a model to account for turbulence. Many of these models use the Boussinesq assumption, which relates the Reynolds stresses to the mean flow using the eddy viscosity [1]. The cost of simplicity in RANS models is the inaccuracy in prediction results for complex flows involving strong flow curvatures, separations, and other complex phenomena [2]. With the rise of data-driven and machine learning techniques, there has been growing interest in the synergy of the two approaches: using experimental data to complement CFD simulations to study and predict turbulent flows [3].

Machine learning methods are a popular strategy used for reconstructing turbulent mean flows with data. These approaches include the *a priori*/CFD-free methods and model-consistent methods. In *a priori*/CFD-free methods the machine learning system is trained directly on inputs and features taken from high-fidelity data to recover discrepancies in the Reynolds stress tensor [4]; examples include eigen-decomposition methods [5–7], neural networks [8] and symbolic regression [9, 10]. A limitation of these approaches is that the model may become inconsistent. This can be the case because differences exist between the features used for training, and those used for prediction, e.g. the DNS quantities for length and time scales do not have a one-to-one correspondence to the RANS equivalents. Secondly, generating detailed high-fidelity data for high Reynolds number flows is challenging. The so-called model-consistent methods developed in parallel can address these issues.

In model-consistent machine learning methods the data-driven model training involves the imperfect RANS environment by explicitly including the baseline model output in the training loss function. This is done by solving a number of inverse problems where the goal is to minimise the discrepancy between the baseline RANS model and measurement data, a so-called *field inversion* approach, sometimes also broadly termed data assimilation [11–13]. Machine-learning algorithms, such as neural networks, can then be used to generalise the discrepancy field for improved

^{*}PhD candidate, Dept. of Automatic Control and Systems Engineering, and Dept. of Mechanical Engineering, obidar1@sheffield.ac.uk

[†]Assistant Professor, Department of Aerospace Engineering, AIAA Senior Member

[‡]Senior Lecturer, Department of Automatic Control and Systems Engineering

[§]Professor, Department of Mechanical Engineering, AIAA Associate Fellow, corresponding author n.qin@sheffield.ac.uk

predictions. Broadly, two streams of field inversion have been pursued in literature: ensemble-based [13–15], and adjoint-based methods [11, 12, 16], both shown to be capable of reconstructing turbulent mean flows given limited, experimentally measurable, data. The focus of this paper is on adjoint-based methods for field inversion because it can recover finer scales compared to the ensemble-based methods.

To date, field inversion using adjoint-based methods has been limited to using only a single source of data. The types of single source data used have included volume data (e.g. velocity profiles [12]), surface data (e.g. skin friction [17], and pressure coefficient [18]), and integral data (e.g. lift coefficient [19])—listed in terms of lowest to highest data sparsity. Using only a single source of data is a limitation because multiple sources can be used simultaneously to train the model and in theory improve the accuracy of the model and ensure that it fits all available data correctly. Zhang et al. [20] have recently demonstrated that the use of ensemble-based field inversion with multiple data sources enhances turbulent mean flow reconstruction. However, a comparable method for using multiple data sources for adjoint-based field inversion is a current research gap that has not yet been addressed.

The aim of this paper is to extend the adjoint-based field inversion framework, a popular data assimilation alternative to ensemble-based methods, to make use of multiple data sources for enhanced turbulent mean flow reconstruction. The approach we take is to use a composite objective function with least squares error terms representing the data for multiple sensors and sources—leading to a weighted least squares optimisation problem. We investigate the multi-objective nature of this optimisation by systematically varying the weighting terms to recover a Pareto-optimal front of the trade-off resulting from differences in weighting the sources of data. We then modify the baseline turbulence model by perturbing the production term of the model transport equation with a spatial scalar field defined at every mesh cell. Subsequently, an optimisation algorithm is employed to find the optimum corrective field that minimises the errors.

In Section II we outline the RANS equations, the baseline Spalart–Allmaras model, and the field inversion formulation. In Section III we use the NASA wall-mounted hump and periodic hill case to compare the novel multi-sensor field inversion against scenarios where data from a single source is used. Finally, the paper is concluded in Section IV.

II. Methods

A. Incompressible RANS equations

The incompressible, steady RANS equations are solved using the `simpleFoam` solver in the popular open-source CFD-code, OpenFOAM:

$$\nabla \cdot \mathbf{U} = 0, \quad (1)$$

$$\nabla \cdot (\mathbf{U}\mathbf{U}) + \nabla p - \nu_{\text{eff}} \nabla \cdot (\nabla \mathbf{U} + \nabla \mathbf{U}^T) = 0, \quad (2)$$

where \mathbf{U} is the velocity, p is the pressure, $\nu_{\text{eff}} = \nu + \nu_t$ is the effective viscosity with ν and ν_t representing the molecular and turbulent kinematic viscosity, respectively.

B. Baseline Spalart–Allmaras model

The one-equation Spalart–Allmaras (S-A) model is chosen as the baseline turbulence model. It models the turbulent kinematic viscosity using the surrogate variable $\tilde{\nu}$, as follows: $\nu_t = \tilde{\nu} f_{\nu 1}$. The transport equation for $\tilde{\nu}$ is [21]:

$$\nabla \cdot (\mathbf{U}\tilde{\nu}) = \underbrace{c_{b1}\tilde{\Omega}\tilde{\nu}}_{\text{production}} + \underbrace{\frac{1}{\sigma} \{ \nabla \cdot [(\nu + \tilde{\nu}) \nabla \tilde{\nu}] + c_{b2} |\nabla \tilde{\nu}|^2 \}}_{\text{transport}} - \underbrace{c_{w1} f_w \left(\frac{\tilde{\nu}}{d} \right)^2}_{\text{dissipation}}, \quad (3)$$

where the intermediate functions are

$$\begin{aligned} f_{\nu 1} &= \frac{\chi^3}{\chi^3 + c_{\nu 1}^3}, & \chi &= \frac{\tilde{\nu}}{\nu}, & f_w &= g \left[\frac{1 + c_{w3}^6}{g^6 + c_{w3}^6} \right]^{1/6}, & g &= r + c_{w2}(r^6 - r), \\ r &= \frac{\tilde{\nu}}{\tilde{\Omega} \kappa^2 d^2}, & \tilde{\Omega} &= \Omega + \frac{\tilde{\nu}}{\kappa^2 d^2} f_{\nu 2}, & f_{\nu 2} &= 1 - \frac{\chi}{1 + \chi f_{\nu 1}}, & c_{w1} &= \frac{c_{b1}}{\kappa^2} + \frac{1 + c_{b2}}{\sigma}, \end{aligned} \quad (4)$$

with Ω representing the rotation rate, and d the wall distance. The model constants are as follows: $c_{b1} = 0.1355$, $c_{\nu 1} = 7.1$, $\sigma = 2/3$, $c_{b2} = 0.622$, $\kappa = 0.41$, $c_{w2} = 0.622$, and $c_{w3} = 2.0$.

C. Field inversion formulation

The baseline model is modified by multiplying a corrective field, β , to the production term in the transport equation for \tilde{v} , Eqn. 3, i.e. $\beta c_{b1} \tilde{\Omega} \tilde{v}$. The optimum discrepancy field, which reduces the functional error in the baseline turbulence model, can be found by minimising an objective function of the following form:

$$\min_{\beta} \mathcal{J} = \left(\sum_{i=1}^{N_d} w_i \frac{1}{\mathcal{J}_{0,i}} \|\mathcal{G}_i(\beta) - \mathbf{d}_i\|_2^2 \right) + \lambda \|\beta - \beta_{\text{prior}}\|_2^2, \quad (5)$$

where $\|\cdot\|_2$ is the $L2$ norm; the index $i \in \mathbb{R}^{N_d}$ represents the different data quantities (e.g. velocity, and pressure); \mathbf{d}_i represents the specific quantity from high-fidelity data, with $\mathcal{G}_i(\beta)$ representing the RANS model equivalent; w_i are the weights; $\mathcal{J}_{0,i}$ are the least-square errors between the baseline model and data; λ is a regularisation parameter, and β_{prior} is typically assumed to be 1, to bias the solution closer the baseline model. The formulation would be ill-posed without the regularisation term because of noisy data and the high degree of freedom in the model compared to the number of data points. We systematically vary the weights w_i to perform a multi-objective optimisation and investigate the trade-off between weighting different sources of data and obtain the Pareto-optimal front describing this trade-off.

D. Adjoint solution and optimisation

The discrete variant of the adjoint formulation is used to efficiently compute the derivatives of the objective function with respect to design variables. An advantage of the discrete adjoint method is the ability to employ automatic differentiation, which is employed in this work, enabled by the open-source DAfoam package [22]. The IPOPT optimisation software [23], based on the interior point line search filter method, is employed for optimisation. For detailed adjoint equations and our open-source implementation of the framework the reader is referred to [24].

III. Results and Discussion

In this section we present the results for two separated flow cases: 1) the 2D NASA wall-mounted hump [25], with available experimental data from the NASA Turbulence Modelling Resource database, and 2) flow over a periodic hill, with detailed LES results from [26]. Both cases involve complex flow features due to separation resulting in discrepancy between eddy viscosity model predictions compared to high-fidelity results. The cases are summarised in Table 1.

Table 1 Summary of cases, where M , Re , C_p , C_f are the Mach number, Reynolds number, surface pressure, and skin friction respectively.

Geometry	Flow conditions	Data	Data type	Data source
2D hump	$M_{\text{ref}} = 0.1$	U_x/U_{ref}	Volume	Experiment
	$Re_c = 936,000$ $C_p = (p - p_{\text{ref}})/0.5\rho U_{\text{ref}}^2$		Surface	
Periodic hill	$M_{\text{ref}} = 0.2$	U_x/U_b	Volume	LES
	$Re_H = 10,595$ $C_f = \tau_w/0.5\rho U_b^2$		Surface	

A. 2D NASA wall-mounted hump

This case involves flow separation, as a result of adverse pressure gradients, over a smooth hump surface, shown in Fig. 1. Linear eddy viscosity models, such as Spalart–Allmaras, are known to poorly predict the separation, reattachment and boundary recovery by over-predicting the size of the separation bubble due to under-predicted turbulent shear stress in the separated region. The available data include experimental surface pressure, and velocity profiles near the hump. The flow conditions are summarised in Table 1. For field inversion we use the surface pressure data in the region $-0.8 \leq x/c \leq 2.1$, and four streamwise velocity profiles as shown in Fig. 1. The objective function is:

$$\mathcal{J} = \underbrace{\frac{w_u}{\mathcal{J}_{0,u}} \sum_{i=1}^{N_d^u} [U_{x,i}(\beta) - U_{x_{\text{data},i}}]^2}_{\mathcal{J}_u} + \underbrace{\frac{w_p}{\mathcal{J}_{0,p}} \sum_{j=1}^{N_d^p} [C_{p,j}(\beta) - C_{p_{\text{data},j}}]^2}_{\mathcal{J}_p} + \lambda \sum_{k=1}^{N_m} [\beta_k - 1]^2, \quad (6)$$

where $w_u + w_p = 1$, and the regularisation constant λ is set to 10^{-6} . To simulate the flow, we solve the incompressible, two-dimensional, steady Navier–Stokes equations on a structured mesh, shown in Fig. 1.

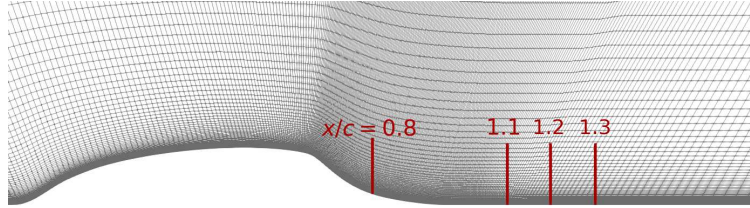


Fig. 1 Close-up of the hump mesh from NASA Turbulence Modelling Resource.

Fig. 2 shows the root-mean-squared error in velocity and surface pressure predictions. It is clear that the total error can be significantly reduced by all field inversion scenarios. The least effective field inversion scenarios are when using data for only one quantity, as expected, although the reconstruction with velocity data is more effective than pressure data. Broadly, the field inversion scenarios with multi-sensor data lead to similar *total* error reduction, although there are clear differences in *individual* quantities. We observe that, generally, a larger weight for a particular quantity leads to a large error reduction for that quantity, and vice-versa, as intuitively expected.

A comparison of the individual objective function terms \mathcal{J}_u and \mathcal{J}_p is shown in Fig. 3. It broadly shows an emerging Pareto front for the multi-objective optimisation, demonstrating the need for a trade-off between the two objectives: one of terms in the composite objective function degrades when the other is improved. According to both figures, the best case scenario is with the weights, $(w_u, w_p) = (0.3, 0.7)$. However, this is not far superior to equally weighting the objective function terms, thus it could be argued that equal weights is sufficient, for this case.

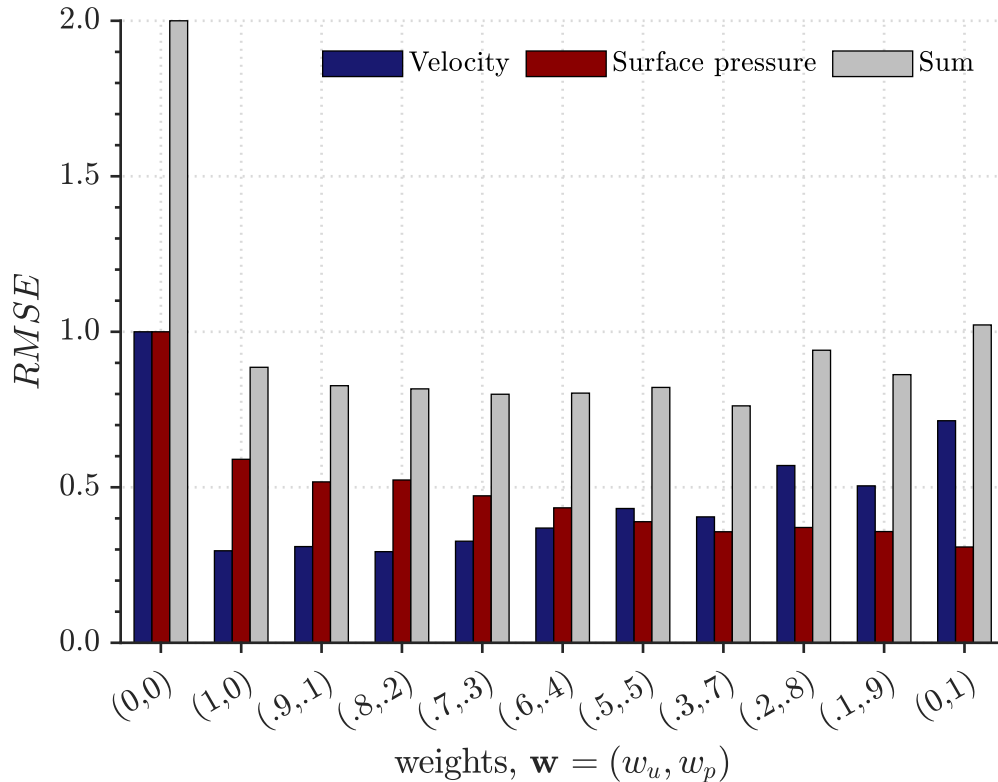


Fig. 2 The root-mean-squared error for the 2D hump for the baseline model (labelled as $\mathbf{w} = (0, 0)$), and various field inversion scenarios. The RMSE values are normalised by the respective RMSE values of the baseline model.

Next, we will compare the baseline and field inversion results (with single and equally-weighted multi-sensor data) in more detail. Fig. 4 shows the surface pressure distribution. It is clear that the S-A model struggles to accurately

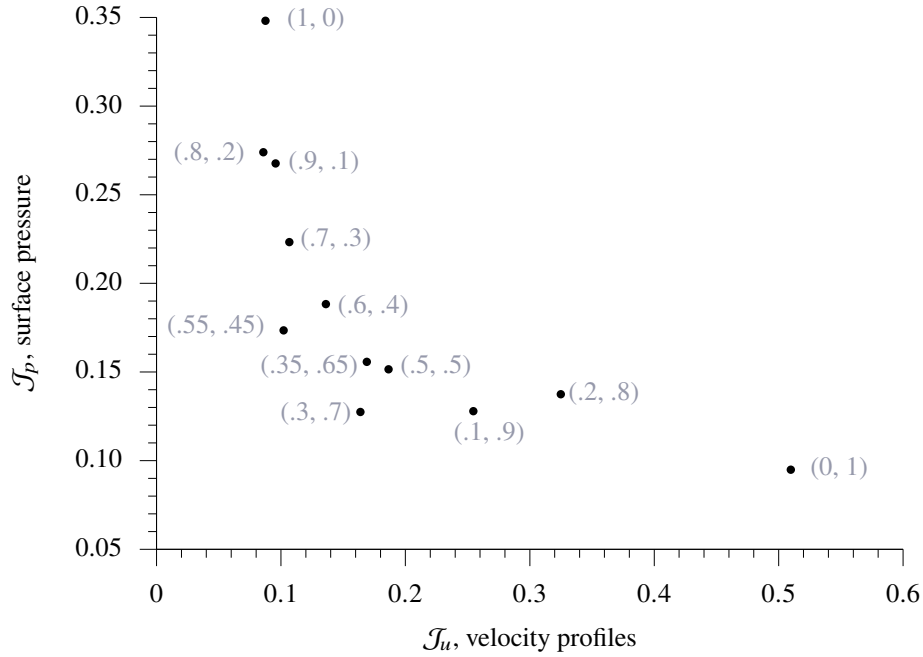


Fig. 3 The Pareto front plot for the 2D hump. The weights are provided next to markers: weights, $w = (w_u, w_p)$.

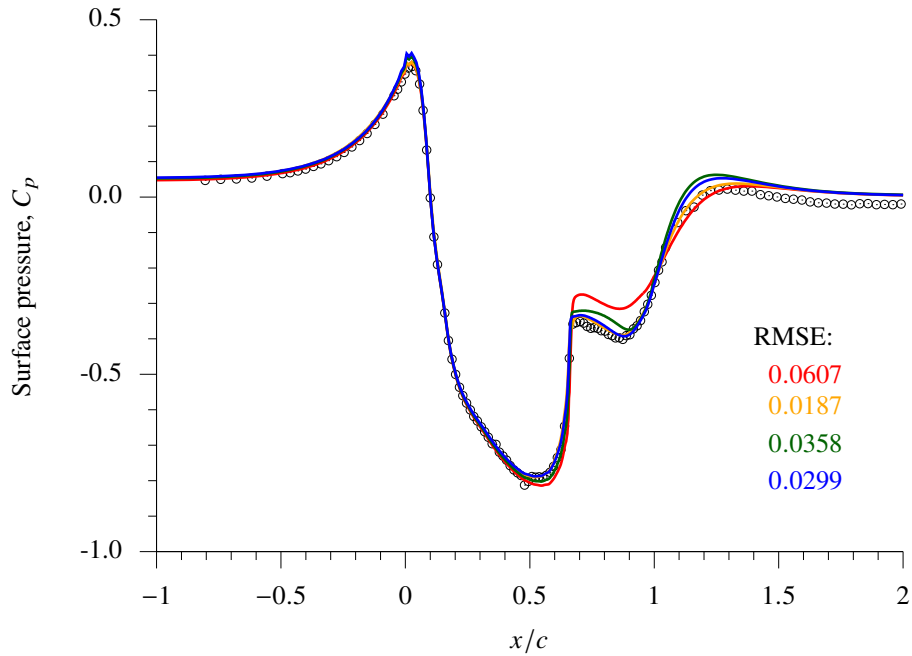


Fig. 4 Comparison of surface pressure on the hump wall. Legend: Experiment (\circ), Spalart-Allmaras (—); field inversion, C_p data (—); field inversion, U_x profile data (—); and field inversion, equally weighted C_p and U_x profile data (—). The RMSE label refers to the root-mean-squared error between the simulation and experimental data, with values colour-coded to match the legend.

predict the pressure in the separated shear layer, which is improved by all three field inversion scenarios. However, there is still some error in the pressure distribution when using velocity profiles alone.

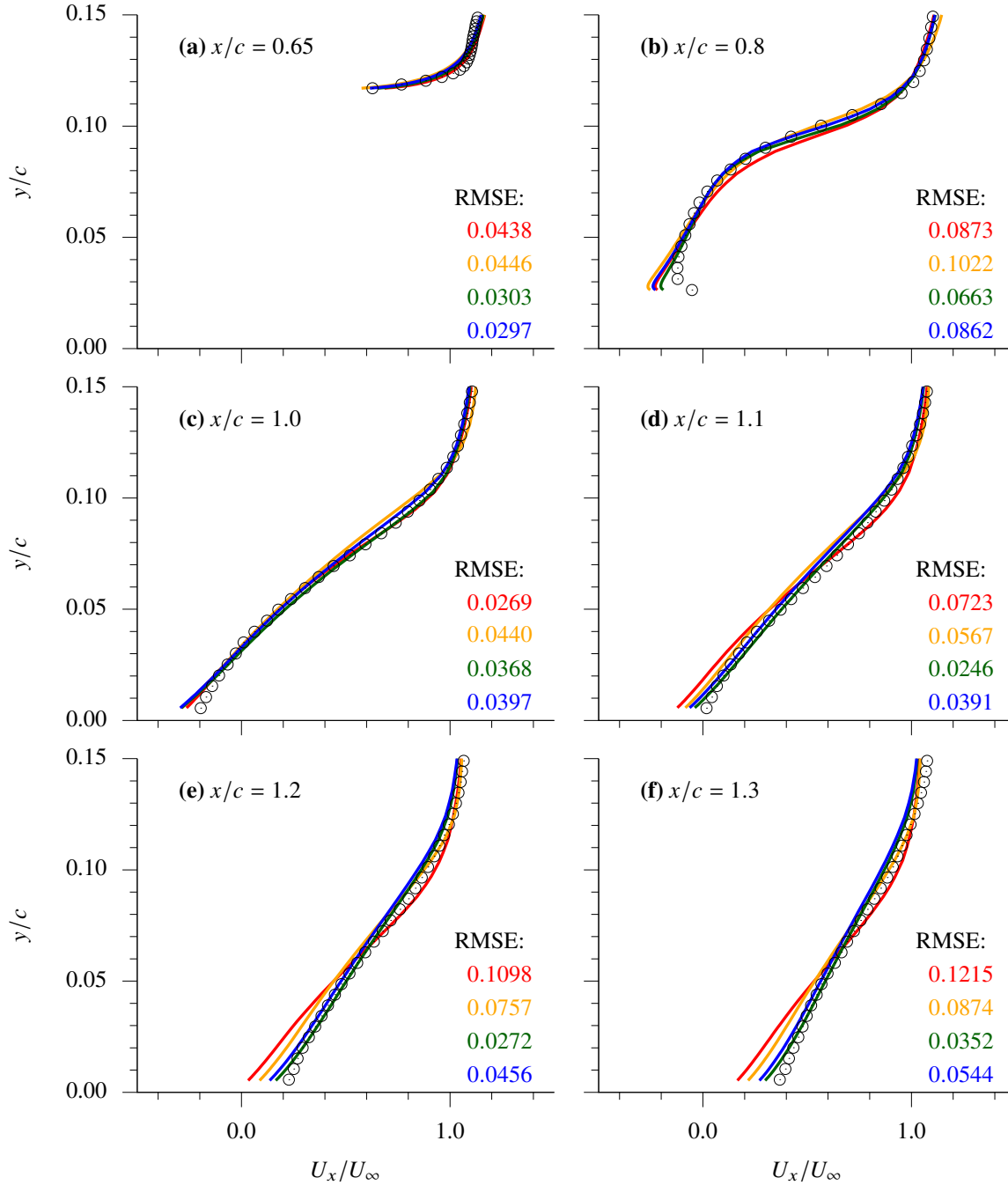


Fig. 5 Comparison of velocity profiles in the 2D hump separation bubble. Legend: Experiment (\circ), Spalart-Allmaras (---); field inversion, C_p data (---); field inversion, U_x profile data (---); and field inversion, equally weighted C_p and U_x profile data (---). The RMSE label refers to the root-mean-squared error between the simulation and experimental data for each velocity profile location, with values colour-coded to match the legend.

The velocity profiles in Fig. 5 show that the baseline model under-predicts the streamwise velocity in the separated shear layer closer to the hump wall. This means that the baseline model predicts a larger separation bubble, and hence delayed reattachment, compared to the experimental data. Performing field inversion with velocity data leads to a more accurate characterisation of the separation, as shown in the velocity profiles. Additionally, it is clear that although the surface pressure data can lead to a very good improvement in the pressure distribution, it is less effective in reducing the

error in the velocity predictions—supporting the case for flow reconstruction based on multi-sensor data.

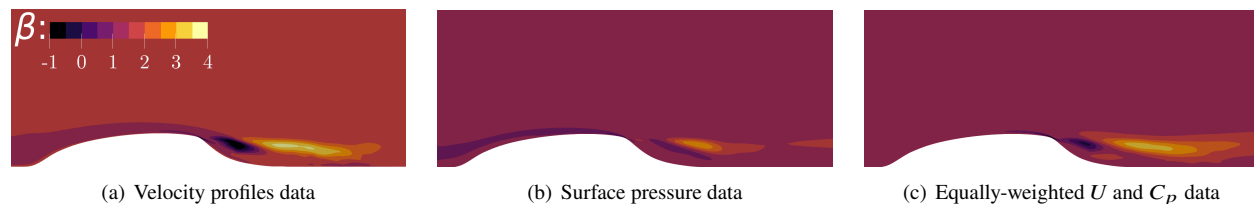


Fig. 6 Comparison of the corrective field, β , for the 2D hump with different field inversion scenarios.

The corrective fields modifying the baseline model to reconstruct the turbulent mean flow is shown in Fig. 6. All cases show a complex distribution where the surrogate turbulence variable, $\tilde{\nu}$, in the S-A model is magnified or dampened, especially in and around the separation. Interpreting the β field with reference to the eddy viscosity ν_t contours in Fig. 7 shows that the various field inversion scenarios increase ν_t in the shear layer which reduces the size of the separation bubble. Negative values of β in the recirculation region and close to the hump wall lead to a reduction of eddy viscosity, hence a slightly delayed separation.

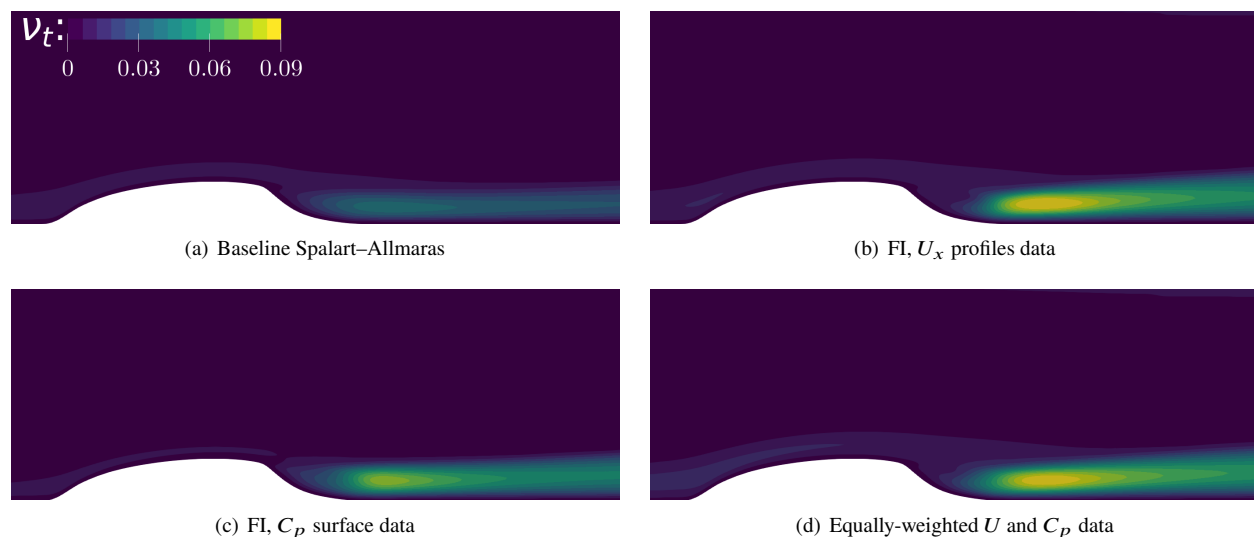


Fig. 7 Comparison of the eddy viscosity, ν_t , for the 2D hump case before and after modifications by β fields shown in Fig. 6.

B. Periodic hill

The periodic hill case, shown in Fig. 8, is a simple geometry comprised of curved surfaces joined by a flat plate. As the flow moves over the first hill, it separates with a large recirculating bubble surrounded by an unsteady shear layer. It then reattaches, and undergoes strong acceleration at the subsequent hill. The flow at the top wall is observed to remain attached with high pressure gradients. These complex features are poorly predicted by RANS turbulence models [27]. Additionally, this case has well defined boundary conditions, and relatively affordable computational cost which has made it an oft-used benchmark case for high-order simulations (LES and DNS), evaluation of RANS turbulence models, and data-driven frameworks. In this work, the LES dataset by Gloerfelt et al. [26] is used for flow reconstruction, with the flow conditions summarised in Table 1.

We use a two-dimensional structured mesh with average $y^+ < 1$ at the walls, taken from the dataset by Xiao et al. [28]. No slip condition is applied at the lower and upper walls, and periodic boundary conditions are used at the hills. A source/forcing term is added to the x -momentum equation to maintain a constant bulk velocity to achieve the LES

Reynolds number, defined as:

$$Re_b = \frac{u_b H}{\nu}, \quad u_b = \frac{1}{2.035H} \int_H^{3.035H} U_x(y) dy, \quad (7)$$

where u_b is the bulk velocity, H is the hills height, ν is the kinematic viscosity, and U_x is the streamwise velocity component.

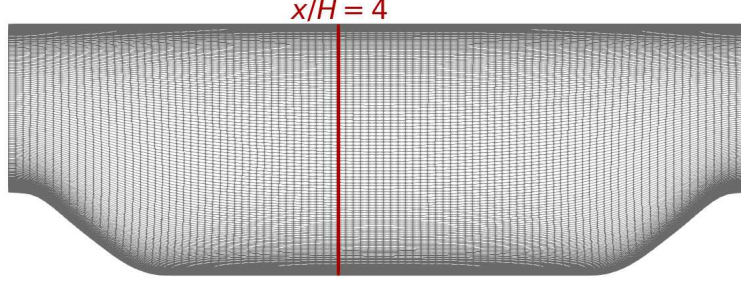


Fig. 8 The structured periodic hill mesh, with approximately 1.5×10^4 cells.

Two sources of data are used for field inversion: 1) vertical continuous slice of streamwise velocity at $x/H = 4$ station (chosen as this is the region close to flow reattachment), and 2) the skin friction in the lower wall, defined as [29]:

$$C_f = \frac{\tau_w}{0.5\rho U_b^2}, \quad \tau_w = \rho \nu \mathbf{t}^T \cdot (\nabla \mathbf{U} \cdot \mathbf{n}), \quad (8)$$

where C_f is the skin friction, τ_w is the wall shear stress, ρ is the fluid density, \mathbf{U} is the velocity, $\mathbf{t} = [t_1, t_2, t_3]^T$ and $\mathbf{n} = [n_1, n_2, n_3]^T$ are the tangential and wall-normal vectors, respectively. The objective function is similar to the hump case, with the C_p term in Eqn. 6 replaced by C_f , and the regularisation constant is set to $\lambda = 10^{-10}$, a very small value to reflect high confidence in the data used for reconstruction.

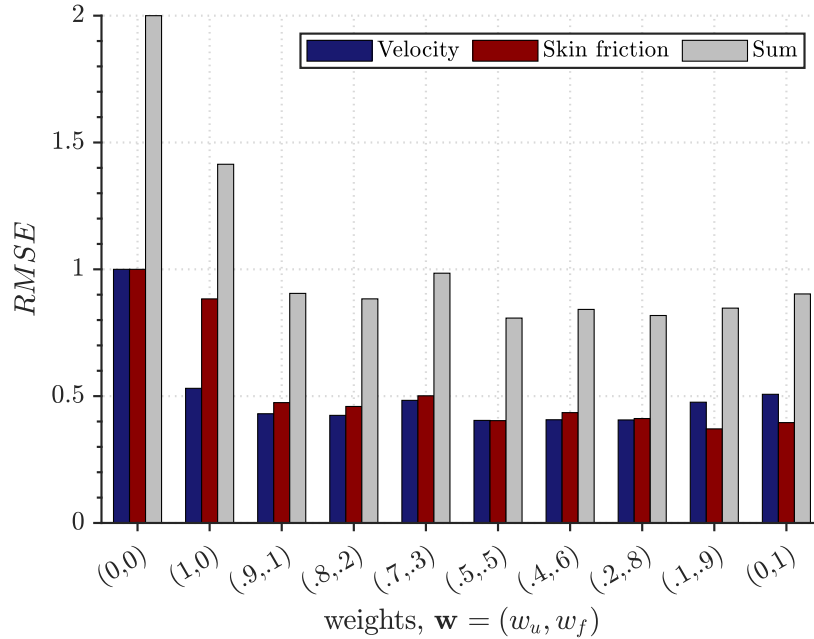


Fig. 9 The periodic hill root-mean-squared error for the baseline model (labelled as $w = (0, 0)$), and various field inversion scenarios. The RMSE values are normalised by the respective RMSE values of the baseline model.

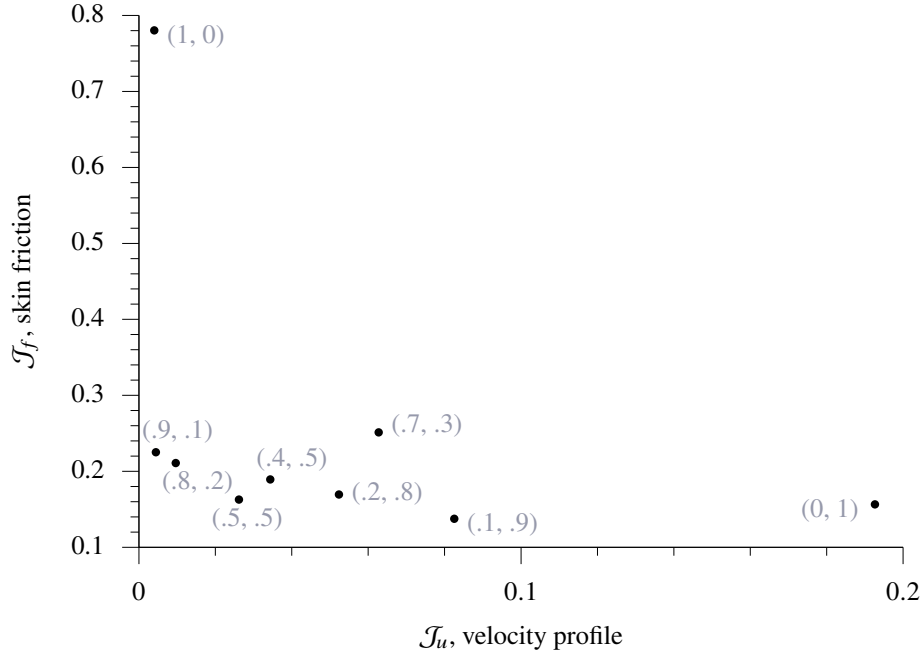


Fig. 10 The Pareto front plot for the periodic hill. The weights are provided next to markers: weights, $w = (w_u, w_p)$.

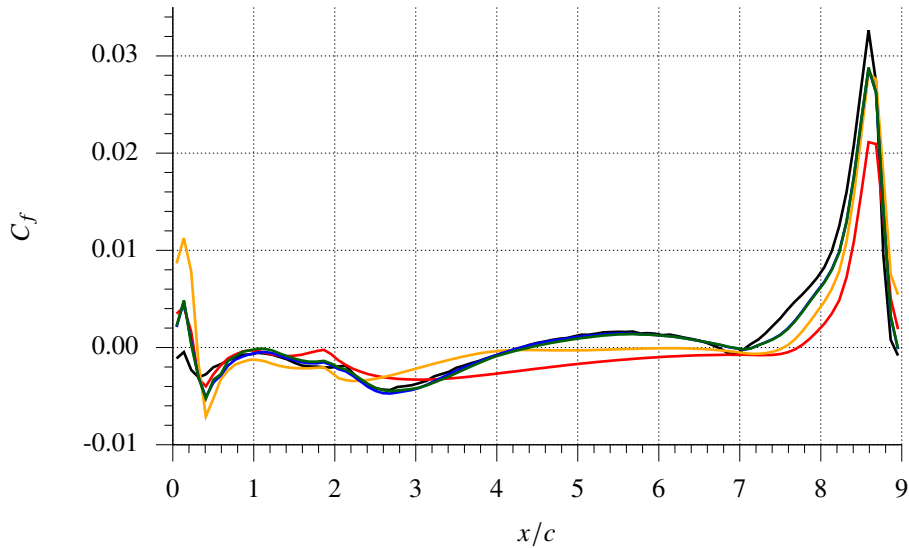


Fig. 11 Comparison of skin friction on the lower wall for the periodic hill case. Legend: LES (—); Spalart–Allmaras (—); FI, U_x profile at $x/H = 4$ (—); FI, C_f (—); and FI, equally weighted with C_f and U_x (—).

Fig. 9 shows that all field inversion scenarios can considerably reduce the root-mean-squared errors for velocity and skin friction prediction compared to the baseline Spalart–Allmaras model. However, using skin friction data on the lower wall is significantly more effective compared to the velocity profile at $x/H = 4$. This is also reflected in the fact that the RMSE is lower for $w_f \geq 0.5$ (i.e. more biased towards fitting C_f data) compared to $w_u \geq 0.5$. The most effective scenario in terms of RMSE error reduction is when the individual data terms in the objective function (i.e. J_u and J_f) are equally-weighted.

Fig. 10 shows a comparison of the individual objective terms, \mathcal{J}_u and \mathcal{J}_f , for different weights. In contrast to the hump case, this case does not necessarily show a clear conflict between minimising the individual terms in the objective function. While in the hump case the error reduction in an individual objective function term is proportional to the weight, in the periodic hill case this is not as clear. In fact, field inversion scenarios with multi-sensor data can lead to further error reduction in both objectives compared to data from a single source (unlike the hump case). This is expected as C_f is a function of the velocity derivative at the wall, as shown in Eqn. 8.

A comparison of the skin friction predictions by the baseline model and field inversion scenarios with C_f data, velocity profile, and both (equally-weighted) is shown in Fig. 11. The baseline model significantly over-predicts the size of the separation bubbles, and thus a very delayed flow reattachment. The field inversion scenarios with skin friction data, and equally weighted velocity profile and C_f data, significantly improve the prediction of separation and reattachment between $1 \leq x/H \leq 4$. Neither the baseline model, nor the different field inversion scenarios capture the slight separation at the initial hill crest, but all field inversion scenarios show improved C_f peak predictions on the second hill, compared to the baseline case. Flow reconstruction with a single velocity profile at $x/H = 4$ is insufficient to capture the complex flow characteristics in the near-wall region, although it does improve it compared to the baseline, by reducing the size of the separation bubble—a mild separation is still observable in and after the location the LES data suggests flow reattachment.

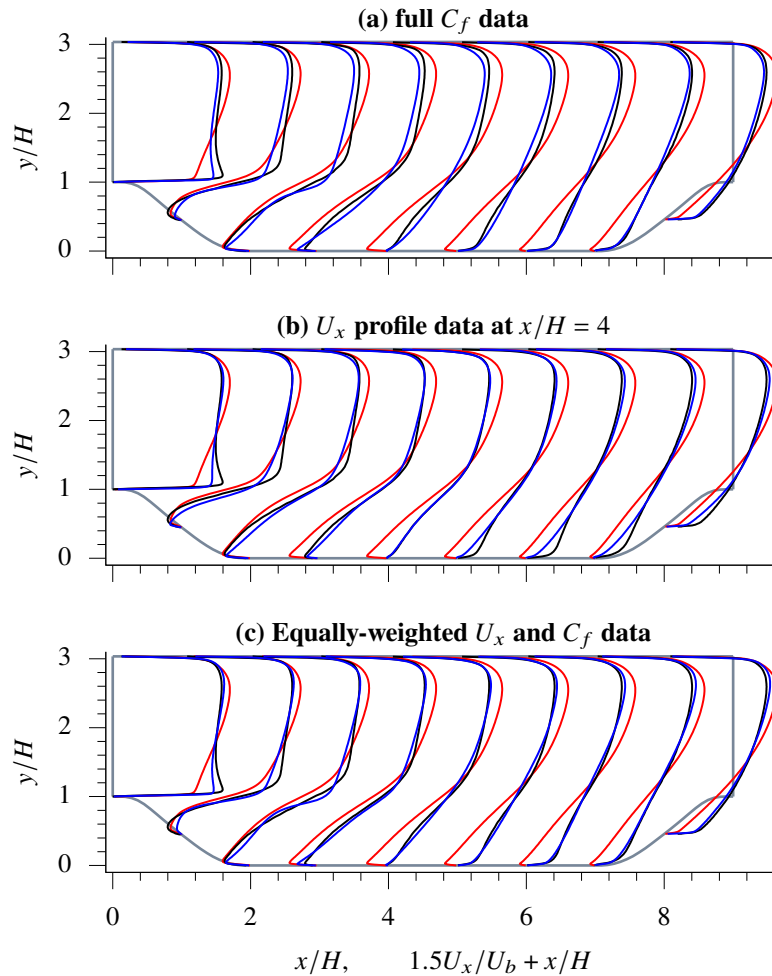


Fig. 12 Comparison of velocity profiles for the periodic hill case. Legend: LES (—), Spalart–Allmaras (—), and field inversion (—).

The velocity profiles shown in Fig. 12 show that field inversion with C_f data can highly improve the near wall (lower) velocity predictions. But, the effect away from the wall is diminished, notably towards the first-half of the domain. On the other hand, using the velocity profile can lead to improved velocity prediction through the majority

of the domain, except some errors in the near wall region prior the second hill. It is clear that when combining both datasets, the velocity predictions can be significantly improved throughout the domain.

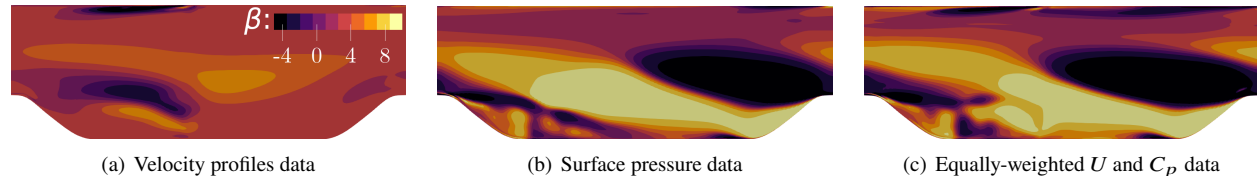


Fig. 13 Comparison of the corrective field, β , for the periodic hill with different field inversion scenarios.

The corrective fields modifying the baseline S-A transport equation is shown in Fig. 13. All three field inversion scenarios show substantial changes to $\tilde{\nu}$ (thus ν_t) throughout the domain, with considerable variations of β in the separated shear layer. In the least effective case (field inversion with velocity profile data) the eddy viscosity (Fig. 14a) is increased in most of the domain, with reduction ($\beta \leq 0$) above the recirculation zone, and the boundary layer in the top wall. In the other two cases, there are drastic magnifying of eddy viscosity in/surrounding the shear layer (Fig. 14 b and c), while eddy viscosity is reduced around the crest of the second hill (Fig. 13 b and c).

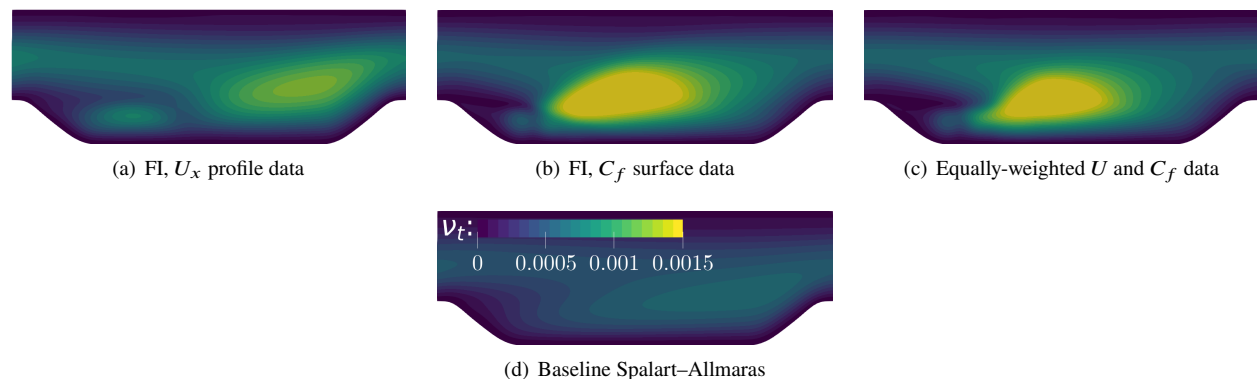


Fig. 14 Comparison of the eddy viscosity, ν_t , for the periodic hill before and after modifications by β fields shown in Fig. 13.

Similar to the hump case, the baseline Spalart–Allmaras model under-predicts the eddy viscosity in the separated shear layer, causing a large separation bubble (hence, delayed flow reattachment). Given enough data, field inversion can remedy this issue, as demonstrated.

IV. Conclusion

In this paper the enhanced capability of turbulent mean flow reconstruction using multi-sensor data was demonstrated for two flows involving strong pressure gradients and flow separation. The variational/adjoint-based field inversion involved modification of the Spalart–Allmaras turbulence model through a spatial corrective field introduced in the model transport equation. The chosen method has the advantage of model consistency over off-the-shelf machine learning algorithms used directly on high-fidelity data without the baseline model, and is able to recover finer scales compared to ensemble-based methods. The two cases tested showed that when using multi-sensor data, equally-weighting the individual terms in the objective function is appropriate. It was also shown that the baseline Spalart–Allmaras model under-predicts the eddy viscosity in the separated shear layer, which results in a larger separation bubbles than observed in high-fidelity data. In the wall-mounted hump case we observed that velocity profiles were more effective in reconstructing turbulent flow compared to surface pressure. On the other hand, the periodic hill case was more sensitive to skin friction (velocity derivative) data, compared to the streamwise velocity profile.

Acknowledgement

Omid Bidar's work is funded by the University of Sheffield Engineering and Physical Sciences Research Council (EPSRC) Doctoral Training Partnership Scholarship.

References

- [1] Launder, B. E., and Sandham, N. D. (eds.), *Closure Strategies for Turbulent and Transitional Flows*, Cambridge University Press, 2001. <https://doi.org/10.1017/cbo9780511755385>.
- [2] Spalart, P. R., and Venkatakrishnan, V., "On the role and challenges of CFD in the aerospace industry," *The Aeronautical Journal*, Vol. 120, No. 1223, 2016, pp. 209–232. <https://doi.org/10.1017/aer.2015.10>.
- [3] Duraisamy, K., Iaccarino, G., and Xiao, H., "Turbulence Modeling in the Age of Data," *Annual Review of Fluid Mechanics*, Vol. 51, No. 1, 2019, pp. 357–377. <https://doi.org/10.1146/annurev-fluid-010518-040547>.
- [4] Duraisamy, K., "Perspectives on machine learning-augmented Reynolds-averaged and large eddy simulation models of turbulence," *Physical Review Fluids*, Vol. 6, No. 5, 2021. <https://doi.org/10.1103/physrevfluids.6.050504>.
- [5] Tracey, B., Duraisamy, K., and Alonso, J., "Application of Supervised Learning to Quantify Uncertainties in Turbulence and Combustion Modeling," *51st AIAA Aerospace Sciences Meeting including the New Horizons Forum and Aerospace Exposition*, American Institute of Aeronautics and Astronautics, 2013. <https://doi.org/10.2514/6.2013-259>.
- [6] Emory, M., Larsson, J., and Iaccarino, G., "Modeling of structural uncertainties in Reynolds-averaged Navier-Stokes closures," *Physics of Fluids*, Vol. 25, No. 11, 2013, p. 110822. <https://doi.org/10.1063/1.4824659>.
- [7] Wu, J.-L., Xiao, H., and Paterson, E., "Physics-informed machine learning approach for augmenting turbulence models: A comprehensive framework," *Physical Review Fluids*, Vol. 3, No. 7, 2018. <https://doi.org/10.1103/physrevfluids.3.074602>.
- [8] Ling, J., Kurzawski, A., and Templeton, J., "Reynolds averaged turbulence modelling using deep neural networks with embedded invariance," *Journal of Fluid Mechanics*, Vol. 807, 2016, pp. 155–166. <https://doi.org/10.1017/jfm.2016.615>.
- [9] Weatheritt, J., and Sandberg, R., "The development of algebraic stress models using a novel evolutionary algorithm," *International Journal of Heat and Fluid Flow*, Vol. 68, 2017, pp. 298–318. <https://doi.org/10.1016/j.ijheatfluidflow.2017.09.017>.
- [10] Schmelzer, M., Dwight, R. P., and Cinnella, P., "Discovery of Algebraic Reynolds-Stress Models Using Sparse Symbolic Regression," *Flow, Turbulence and Combustion*, Vol. 104, No. 2-3, 2019, pp. 579–603. <https://doi.org/10.1007/s10494-019-00089-x>.
- [11] Duraisamy, K., Zhang, Z. J., and Singh, A. P., "New Approaches in Turbulence and Transition Modeling Using Data-driven Techniques," *53rd AIAA Aerospace Sciences Meeting*, American Institute of Aeronautics and Astronautics, 2015. <https://doi.org/10.2514/6.2015-1284>.
- [12] Parish, E. J., and Duraisamy, K., "A paradigm for data-driven predictive modeling using field inversion and machine learning," *Journal of Computational Physics*, Vol. 305, 2016, pp. 758–774. <https://doi.org/10.1016/j.jcp.2015.11.012>.
- [13] Kato, H., Yoshizawa, A., Ueno, G., and Obayashi, S., "A data assimilation methodology for reconstructing turbulent flows around aircraft," *Journal of Computational Physics*, Vol. 283, 2015, pp. 559–581. <https://doi.org/10.1016/j.jcp.2014.12.013>.
- [14] Xiao, H., Wu, J.-L., Wang, J.-X., Sun, R., and Roy, C., "Quantifying and reducing model-form uncertainties in Reynolds-averaged Navier–Stokes simulations: A data-driven, physics-informed Bayesian approach," *Journal of Computational Physics*, Vol. 324, 2016, pp. 115–136. <https://doi.org/10.1016/j.jcp.2016.07.038>.
- [15] Mons, V., Chassaing, J.-C., Gomez, T., and Sagaut, P., "Reconstruction of unsteady viscous flows using data assimilation schemes," *Journal of Computational Physics*, Vol. 316, 2016, pp. 255–280. <https://doi.org/10.1016/j.jcp.2016.04.022>.
- [16] Singh, A. P., and Duraisamy, K., "Using field inversion to quantify functional errors in turbulence closures," *Physics of Fluids*, Vol. 28, No. 4, 2016, p. 045110. <https://doi.org/10.1063/1.4947045>.
- [17] Duraisamy, K., Singh, A.-P., and Pan, S., "Augmentation of Turbulence Models Using Field Inversion and Machine Learning," *55th AIAA Aerospace Sciences Meeting*, American Institute of Aeronautics and Astronautics, 2017. <https://doi.org/10.2514/6.2017-0993>.
- [18] Belligoli, Z., Dwight, R. P., and Eitelberg, G., "Reconstruction of Turbulent Flows at High Reynolds Numbers Using Data Assimilation Techniques," *AIAA Journal*, Vol. 59, No. 3, 2021, pp. 855–867. <https://doi.org/10.2514/1.j059474>.

- [19] Singh, A. P., Medida, S., and Duraisamy, K., “Machine-Learning-Augmented Predictive Modeling of Turbulent Separated Flows over Airfoils,” *AIAA Journal*, Vol. 55, No. 7, 2017, pp. 2215–2227. <https://doi.org/10.2514/1.j055595>.
- [20] Zhang, X.-L., Xiao, H., He, G.-W., and Wang, S.-Z., “Assimilation of disparate data for enhanced reconstruction of turbulent mean flows,” *Computers & Fluids*, Vol. 224, 2021, p. 104962. <https://doi.org/10.1016/j.compfluid.2021.104962>.
- [21] Spalart, P., and Allmaras, S., “A one-equation turbulence model for aerodynamic flows,” *30th Aerospace Sciences Meeting and Exhibit*, American Institute of Aeronautics and Astronautics, 1992. <https://doi.org/10.2514/6.1992-439>.
- [22] He, P., Mader, C. A., Martins, J. R. R. A., and Maki, K. J., “DAFoam: An Open-Source Adjoint Framework for Multidisciplinary Design Optimization with OpenFOAM,” *AIAA Journal*, Vol. 58, No. 3, 2020, pp. 1304–1319. <https://doi.org/10.2514/1.j058853>.
- [23] Wächter, A., and Biegler, L. T., “On the implementation of an interior-point filter line-search algorithm for large-scale nonlinear programming,” *Mathematical Programming*, Vol. 106, No. 1, 2005, pp. 25–57. <https://doi.org/10.1007/s10107-004-0559-y>.
- [24] Bidar, O., He, P., Anderson, S., and Qin, N., “An open-source adjoint-based field inversion tool for data-driven RANS modelling,” *AIAA 2022 Aviation Forum*, American Institute of Aeronautics and Astronautics, 2022.
- [25] Greenblatt, D., Paschal, K. B., Yao, C.-S., Harris, J., Schaeffler, N. W., and Washburn, A. E., “Experimental Investigation of Separation Control Part 1: Baseline and Steady Suction,” *AIAA Journal*, Vol. 44, No. 12, 2006, pp. 2820–2830. <https://doi.org/10.2514/1.13817>.
- [26] Gloerfelt, X., and Cinnella, P., “Large Eddy Simulation Requirements for the Flow over Periodic Hills,” *Flow, Turbulence and Combustion*, Vol. 103, No. 1, 2019, pp. 55–91. <https://doi.org/10.1007/s10494-018-0005-5>.
- [27] Leschziner, M., “Modelling Separation from Curved Surfaces with Anisotropy-Resolving Turbulence Closures,” *Modelling Fluid Flow*, Springer Berlin Heidelberg, 2004, pp. 23–47. https://doi.org/10.1007/978-3-662-08797-8_2.
- [28] Xiao, H., Wu, J.-L., Laizet, S., and Duan, L., “Flows over periodic hills of parameterized geometries: A dataset for data-driven turbulence modeling from direct simulations,” *Computers & Fluids*, Vol. 200, 2020, p. 104431. <https://doi.org/10.1016/j.compfluid.2020.104431>.
- [29] Krank, B., Kronbichler, M., and Wall, W. A., “Direct Numerical Simulation of Flow over Periodic Hills up to $Re = 10,595$,” *Flow, Turbulence and Combustion*, Vol. 101, No. 2, 2018, pp. 521–551. <https://doi.org/10.1007/s10494-018-9941-3>.